Highly conductive triple network hydrogel thermoelectrochemical cells with low-grade heat harvesting

Yen-Ting Lin [a], Ching-Chieh Hsu [a], Shao-Huan Hong [b], Ling-Chieh Lee [a], U-Ser Jeng [c], Hsin-Lung Chen [d], Shih-Huang Tung [e], Cheng-Liang Liu [a,f,*]

[a] Department of Materials Science and Engineering, National Taiwan University, Taipei, 10617, Taiwan
[b] Department of Chemical and Materials Engineering, National Central University, Taoyuan, 32001, Taiwan
[c] National Synchrotron Radiation Research Center, Hsinchu, 30076, Taiwan
[d] Department of Chemical Engineering, National Tsing Hua University, Hsinchu, 30013, Taiwan
[e] Institute of Polymer Science and Engineering, National Taiwan University, Taipei, 10617, Taiwan
[f] Advanced Research Center for Green Materials Science and Technology, National Taiwan University, Taipei, 10617, Taiwan

HIGHLIGHTS

- Novel quasi-solid thermo-electrochemical cells made of triple-network hydrogel.
- To reveal the nanostructure behavior of thermoelectrochemical cells by SAXS and WAXS.
- High ionic conductivity corelated to nanostructure appearance.
- Excellent wearable electronics performance with 9-series connected TEG.

GRAPHICAL ABSTRACT
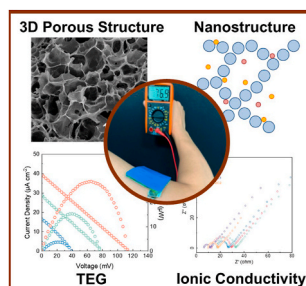
ARTICLE INFO

ABSTRACT

Quasi-solid thermoelectrochemical cells (TECs) are promising candidates for wearable energy harvesting devices as they enable the continuous conversion of low-grade heat into electricity. However, the TEC performance remains limited by inadequate ionic conductivity. Herein, a triple-network hydrogel consisting of poly-acrylamide/poly(vinyl alcohol)/cellulose nanofiber (PAAM/PVA/CNF) is synthesized via a freeze-thaw method, and soaked in the thermogalvanic redox couple $Fe(CN)_6^{3-/4-}$ as the electrolyte. By optimizing the polymer composition and soaking time, a superior ionic conductivity of 168 mS cm^{-1} is achieved while maintaining a thermopower of ~1.69 mV K^{-1}. The high ionic conductivity is provided by the fractal microstructure of the hydrogel, as revealed by small-angle X-ray scattering (SAXS). Moreover, the as-fabricated thermoelectric generator array exhibits an exceptional power output of 28.7 μW at a temperature difference of 11.9 K. This work provides insights on the development of wearable thermoelectric materials for practical and reliable energy harvesting applications.

1. Introduction

In contemporary society, the pressing energy crisis and environmental pollution issues demand immediate attention and resolution [1–6]. To this end, green energy sources have emerged as an effective approach toward sustainable development and long-term viability. Among the available low-grade thermal energy sources such as solar energy, industrial heat, and human body heat, a substantial amount is dissipated into the surrounding environment as waste heat [7–11]. Consequently, there has been growing interest in the advancement of thermoelectric devices that enable the effective capture and utilization of such waste heat. Unlike conventional power sources, thermoelectric devices have the distinct advantage of directly converting heat energy into continuous electricity, thereby eliminating the need for frequent recharging. Extensive research efforts have been devoted to investigating traditional electronic thermoelectric materials, which encompass narrow-bandgap compound semiconductors that employ either electrons or holes as charge carriers, with the aim of enhancing their performance and capabilities [12–16]. Nevertheless, the widespread applications of conventional inorganic thermoelectric materials are limited by their potential toxicity, brittleness, limited flexibility, and high cost [17–21]. Additionally, these materials typically exhibit low thermopowers on the scale of microvolts per kelvin, which necessitates the integration of numerous thermoelectric units or additional voltage amplifiers to achieve the desired voltage output for small temperature differentials [22–27]. Hence, thermoelectrochemical cells (TECs) have recently gained considerable attention due to their affordability and comparatively high thermopowers on the scale of millivolts per kelvin [28–36]. A TEC consists of two inert electrodes and an electrolyte solution containing a redox couple. The temperature-dependent redox reaction that occurs during electron transfer between the redox couple and electrodes enables steady energy conversion. Various redox couples, such as $Fe^{2+/3+}$ [37–39], I^-/I^{3-} [40,41], $Co_{II/III}(bpy)_3^{2+/3+}$ [42], and $Sn^{2+/4+}$ [31] have been used in liquid-state TECs to achieve milliwatt outputs and relatively high energy conversion efficiencies even under small temperature gradients. However, the practical application of liquid TECs has been hindered by leakage issues. To address this challenge, hydrogel-based quasi-solid TECs have been developed that encapsulate the redox couples in polymer networks. Quasi-solid TECs incorporating polymer matrices such as gelatin [43], poly(vinyl alcohol) (PVA) [44], polyacrylamide (PAAM) [45,46], polyvinylidene difluoride (PVDF) [42], and cellulose [47–49] have been successfully developed, thereby enabling the realization of flexible power supplies [50,51]. Nevertheless, the energy harvesting capability and potential applications of the hydrogel system are restricted by the complex encapsulation processes and suboptimal thermoelectrochemical properties, with a thermopower of approximately 1 mV K^{-1} and a low ionic conductivity of a few millisiemens per centimeter [52–56]. As a result, the focus of recent research has shifted towards developing flexible TECs with enhanced thermoelectric performances, especially in terms of the ionic conductivity.

Herein, TECs are developed based on a triple-network structure of polyacrylamide/poly(vinyl alcohol)/cellulose nanofiber (PAAM/PVA/CNF). These TECs are specifically tailored for the high-efficiency harvesting of low-grade thermal energy by utilizing the ferro/ferricyanide $Fe(CN)_6^{3-/4-}$ ion redox couple. A novel application of small-angle X-ray scattering (SAXS) to the hydrogel system reveals the controlled nanostructure of the TECs that is obtained via the optimized polymer composition and appropriate redox solution soaking time. As a result, the TEC exhibits a superior ionic conductivity of 168 mS cm^{-1}, a high power factor (PF) of 47.9 μW m^{-1} K^{-2}, and a figure of merit (zT) of 0.06. To further showcase the potential of the optimized TEC, a 3 × 3 thermoelectric generator (TEG) array is assembled and shown to provide a high output current of 1.0 mA, an output voltage of 113.1 mV, and a power density of 14.2 mW m^{-2} at a temperature difference of 11.9 K. Moreover, the TEG array delivers a stable voltage when attached to the human skin, yielding a voltage output of 76.9 mV at an ambient temperature of 298.15 K. This successful demonstration highlights the feasibility of the proposed strategy for practical wearable power generation applications.

2. Experimental section

2.1. Materials

Acrylamide (AAM) monomer, ammonium persulfate (APS), N,N′-methylenebisacrylamide (MBAA), poly(vinyl alcohol) (PVA, MW = 89000–98000), boric acid (borax), potassium ferricyanide (K$_3$Fe(CN)$_6$), potassium hexacyanoferrate (II) (K$_4$Fe(CN)$_6$·3H$_2$O) and polydimethylsiloxane (PDMS, base: crosslinker = 10:1) were purchased from Sigma-Aldrich. Cellulose nanofiber (CNF) with a weight percentage of 3 wt % was purchased from Process Development Center (PDC) of The University of Maine.

2.2. Preparation of double-network (DN) or triple-network (TN) hydrogel samples

Initially, a PAAM solution was prepared by dissolving 3 g of AAM monomer and 5 mg of APS initiator in 15 mL of deionized (DI) water. Simultaneously, a PVA solution prepared by dissolving 1 g of PVA powder in 10 mL of DI water. The DN and TN hydrogels were synthesized using a one-pot method. In the case of the DN hydrogel, the PAAM and PVA solutions were combined, while for the TN hydrogel, the PAAM, PVA, and CNF dispersion were mixed. The specific mixing ratios for each component are provided in Table 1. The resulting mixture was stirred for 30 min. To initiate crosslinking, MBAA and a 0.1 M borax solution were incrementally added to the mixture according to the prescribed ratios mentioned in Table 1. The solution was further stirred for an additional 30 min. Subsequently, the mixed solution was subjected to heating at a temperature of 70 °C for 5 h to facilitate thermopolymerization of the PAAM. This was followed by the implementation of a one cycle freeze-thaw method between temperatures of −40 °C and 25 °C, to obtain either DN or TN hydrogel samples.

2.3. Preparation of thermoelectrochemical cells (TECs)

To obtain DN or TN TECs, the prepared DN or TN hydrogel samples were soaked in a K$_{3/4}$Fe(CN)$_6$ solution in DI water with concentrations of 0.25/0.42 M for 24 h. And different soaking times from 30 s to 24 h were employed to facilitate further investigation.

Table 1
Composition of double-network (DN) and triple-network (TN) hydrogel samples, PVA solution were prepared with mass concentration of 10 wt%, borax solution were prepared with molar concentration of 0.1 M.

Sample	AAM solution (mL)	PVA solution[a] (mL)	CNF dispersion (g)	MBAA[b] (mg)	Borax solution[c] (mL)
DN-V1	1	1	0	0.1	0.67
DN-V2	1	2	0	0.1	1.34
TN-V1C1	1	1	0.1	0.1	0.67
TN-V2C1	1	2	0.1	0.1	1.34
TN-V2C2	1	2	0.2	0.1	1.34

[a] The PVA solution was prepared with mass concentration of 10 wt%.
[b] The adding amount of MBAA crosslinker was fixed in the concentration of 0.1 mg/mL to PAAM solution.
[c] The adding volume of borax solution was fixed in the ratio to PVA solution in 2/3 mL vol/vol.

2.4. Fabrication of TEG array

Firstly, a PDMS mold was created with 3×3 square array, where each rectangle were fixed at dimensions of 1.5×1.5 cm^2 and a height of 0.3 cm. The prepared TN-V2C1 TECs were cut into $1.5 \times 1.5 \times 0.3$ cm^3 and placed into PDMS mold. Each piece were connected by Ni electrodes to form the TEG array. Finally, the TEG array was encapsulated using thermoconductive tape.

2.5. Thermoelectrochemical performance measurements

The thermoelectrochemical performance measurements for both TECs and TEG array were conducted using a specific apparatus. The setup consists of two Peltier units positioned in vertical direction, capable of functioning independently as the hot and cold parts. The temperature of hot section was controlled by customized temperature controller, while the temperature of cold section was controlled by water bath. To measure the temperatures at both ends of the thermoelectric generators (with Ni electrode used for all thermoelectrochemical measurements), two thermocouples were employed. The measurements were carried out using a Keithley 2400 source meter/voltmeter/data acquisition in conjunction with a customized temperature recorder.

3. Results and discussion

3.1. Preparation of double-network (DN) and triple-network (TN) hydrogel samples

The step-by-step preparation process of the TN TEC is shown schematically in Fig. 1. First, the formation of polyacrylamide (PAAM) chains was prepared via a radical polymerization process using acrylamide (AAM) as the monomer and ammonium persulfate (APS) as the initiator. Meanwhile, a poly(vinyl alcohol) (PVA) solution was prepared separately by dissolving the PVA powder in deionized (DI) water. The two polymer solutions were then mixed with a cellulose nanofiber (CNF) dispersion. N,N′-methylenebisacrylamide (MBAA) and borax were used as crosslinkers for the PAAM and PVA, respectively. Thermo-crosslinking and freeze-thaw processes were performed out to obtain the triple-network TN hydrogel samples, wherein the PAAM network provides shape construction ability via strong crosslinking interactions with MBAA, while the PVA network imparts flexibility through its mobile polymer chains within the hydrogel, and the CNF network interpenetrates the PAAM and PVA polymer chains to enhance the mechanical properties of the hydrogel, as demonstrated in Figs. S1a–c of the Supplementary Material.

To fabricate the TN TEC, the TN hydrogel samples were immersed in an $Fe(CN)_6^{3-/4-}$ redox solution. As shown in Figs. S1d–f, the excellent

mechanical properties of the as-fabricated TN TECs were demonstrated via stretching and twisting tests. The same procedures were followed, but without the addition of CNF, to obtain pristine DN hydrogel samples and DN TECs, as shown in Fig. S2. A complete list of all hydrogel samples and their corresponding components is provided in Table 1. Thus, the DN hydrogel samples designated DN-V1 and DN-V2 were prepared using 1-mL and 2-mL PVA solutions, respectively, at a fixed PAAM concentration of 0.1 mg/mL, while the TN hydrogel samples designated TN-V1C1, TN-V2C1, and TN-V2C2 were prepared using PVA/CNF ratios of 1 mL/0.1 g, 2 mL/0.1 g and 2 mL/0.2 g, respectively, at a fixed AAM concentration of 0.1 mg/mL.

3.2. Molecular interactions, morphologies, and mechanical properties

The molecular structures of the various hydrogel samples are revealed by the attenuated total reflectance Fourier transform infrared (ATR-FTIR) spectra in Fig. 2a. Here, the characteristic FTIR bands of the hydrogel samples remain relatively consistent across the various compositions. In detail, the bands at 3390 cm^{-1} and 3225 cm^{-1} correspond to the symmetrical stretching vibrations of the –OH groups and N–H bonds, respectively. Additionally, the bands at 1643 cm^{-1}, 1424 cm^{-1}, and 1140 cm^{-1} correspond to the symmetric stretching vibrations of the C = O bonds, –NH$_2$ groups, and B–O–C bonds, respectively. Notably, the bands at 3390 cm^{-1} exhibit stronger peaks as the concentrations of either PVA or CNF are increased (Fig. S3a), thus indicating an increased quantity of –OH groups. However, the bands at 3225 cm^{-1} remain nearly unchanged, thereby indicating a consistent amount of PAAM in the hydrogel samples. Furthermore, the stretching vibrations of the B–O–C bonds exhibit increasing peak intensities as the amount of borax solution is increased (Fig. S3b).

The morphologies of the hydrogel samples are elucidated by the cross-sectional field-emission scanning electron microscope (FESEM) images of the freeze-dried DN and TN hydrogel samples in Fig. 2b–f. Here, each sample exhibits an interconnected reticular porous microstructure that should provide favorable ion transport characteristics when employed with an electrolyte. Upon the addition of the CNF filler, however, the TN-V1C1, TN-V2C1, and TN-V2C2 hydrogel samples each exhibit a more organized arrangement (Fig. 2d–f). Moreover, these three-dimensional (3D) framework samples exhibit enhanced mechanical stability during stretching or twisting (Figs. S1a–c), thereby potentially improving the thermoelectrochemical performance, due to the presence of a well-defined pore structure. These findings are supported by the lower magnification images in Fig. S4, thereby indicating the excellent homogeneity of the various hydrogel samples.

The rheological properties of the various hydrogels within the temperature range of 20–40 °C are revealed in Fig. 3a. Here, all of the hydrogel samples maintain their quasi-solid states throughout the temperature range, as indicated by the storage modulus (G′) being higher
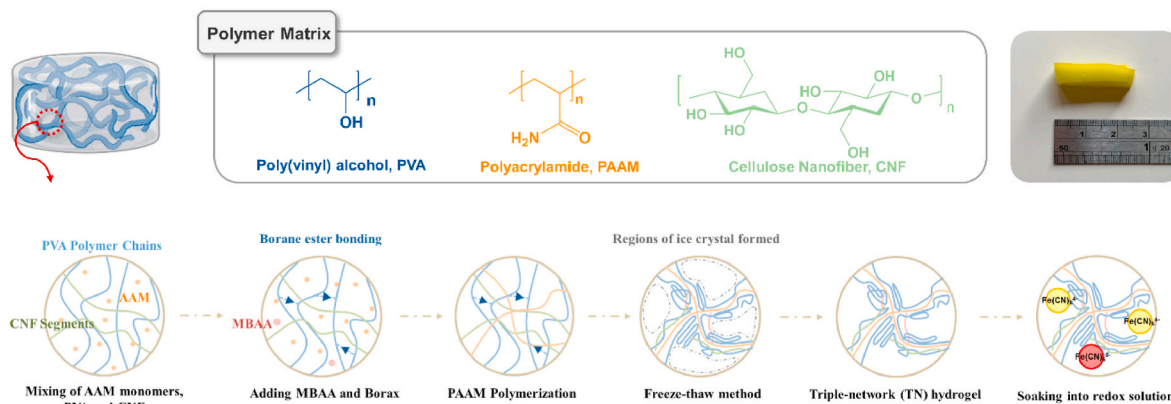

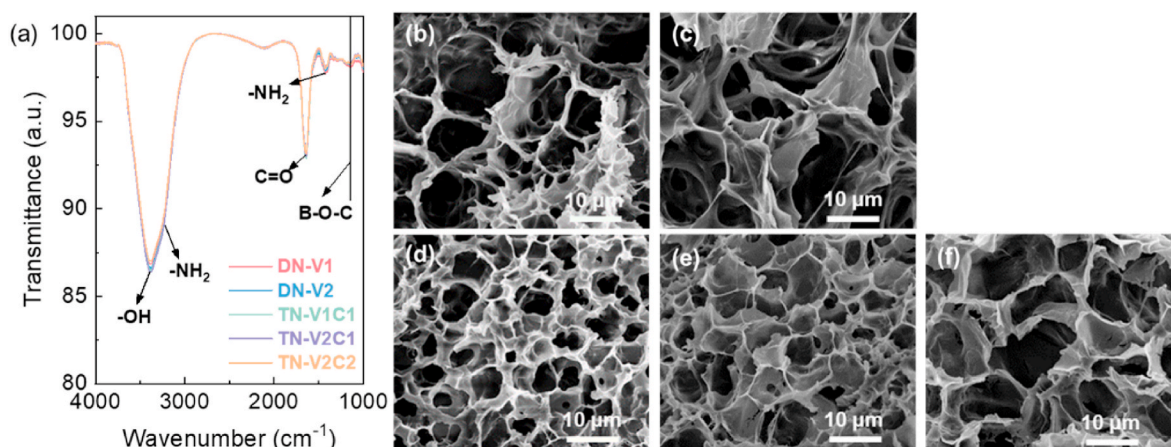**Fig. 1.** Schematic illustration of TN TECs preparation process and corresponded optical image.

Fig. 2. Molecular and morphology characterization of pristine hydrogel samples. (a) ATR-FTIR full spectra, SEM images of (b) DN-V1, (c) DN-V2, (d) TN-V1C1, (e) TN-V2C1 and (f) TN-V2C2.
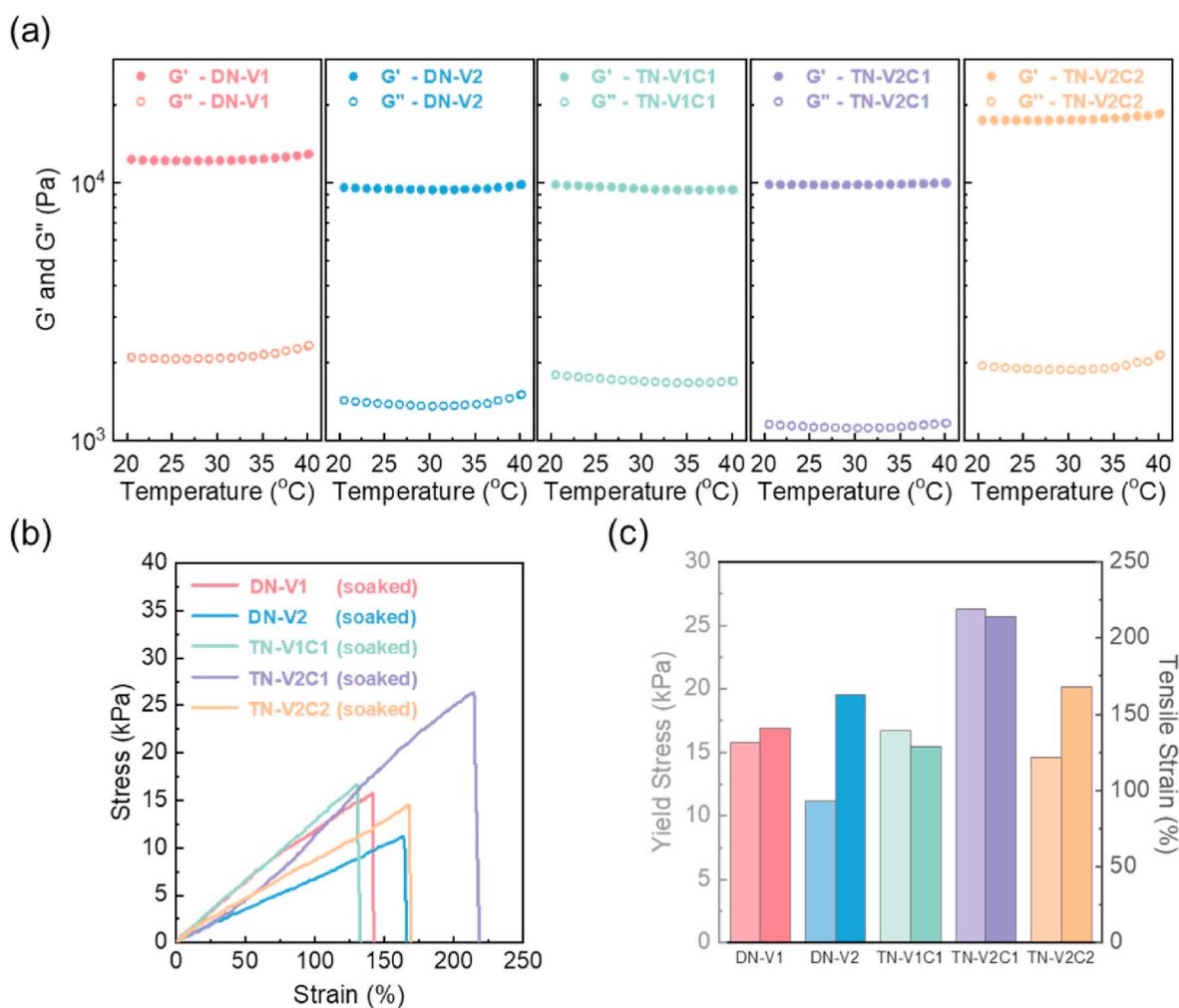

Fig. 3. Mechanical properties of pristine hydrogel samples and TECs. (a) Rheology analysis under the temperature range from 293.15 K to 313.15 K for pristine hydrogel samples, (b) stress-strain curve of TECs, and (c) yield stress and tensile strain comparison along with various TECs.

than the loss modulus (G''). Moreover, the values of G' and G'' remain relatively constant as the temperature increases. These results indicate the stability of the 3D hydrogel framework within the operational temperature range, thereby ensuring a consistent ion transport channel as a TEC. Notably, the CNF filler plays a vital role in significantly

influencing the mechanical properties by causing a larger difference between the G' and G'' values in the TN hydrogel samples, as confirmed by the stretching test results in Figs. S5a and b. In the absence of CNF, the tensile strains of the DN-V1 and DN-V2 hydrogel samples increase from 160 % to 176 %, respectively (Figs. S5a and b). In the presence of

CNF, however, the yield stress is enhanced by the reinforced morphological structure, as demonstrated in Fig. 2d–f and Figs. S4c–e. Moreover, the TN-V2C1 hydrogel sample exhibits the best mechanical properties of all, with a yield stress of 25.7 kPa and a tensile strain of 228 %, thereby demonstrating that this is the optimum composition. The optimal mechanical properties observed in TN-V2C1 are attributed to a balanced polymer concentration. The moderate concentration of polymer, when combined with PVA, contributes to expansion and softness, while the incorporation of CNF provides toughness within the hydrogel matrix. It should be noted that excessive amounts of either PVA or CNF may compromise mechanical attributes such as yield stress or strain, respectively.

As shown in Fig. 3b and **c** and Fig. S5c, the TECs maintain good mechanical properties even after being soaked in the redox solution, although there is a slight increase in the yield stress and a slight decrease in the tensile strain. For example, the TN-V2C1 TEC exhibits a yield stress of 26.3 kPa and a tensile strain of 214 % after soaking, compared to 25.7 kPa and 228 % before soaking. This can be attributed to the weakened interactions between the polymer and water molecules due to solvent exchange between the deionized (DI) water and the redox solution. Taken together, the above results indicate that the hydrogel-based TECs maintain adequate mechanical properties, thus making them suitable for applications in wearable electronics.

3.3. Electrochemical and thermoelectrochemical properties

The electrochemical properties of the TECs in a two-electrode system with thin-film platinum electrodes are revealed in Fig. 4. Here, the various TECs each exhibit similar reduction and oxidation peaks in the cyclic voltammetry (CV) curves obtained at a scan rate of 10 mV s^{-1} (Fig. 4a), corresponding to the Fe(CN)$_6^{3-/4-}$ redox couple, thereby indicating excellent electrochemical activity within the hydrogel matrix.

However, the reduction peak of the DN-V1 TEC and the oxidation peak of the TN-V1C1 TECs exhibit slightly broader and less symmetric peak shapes. This can be attributed to the lower amounts of PVA in these samples, which are insufficient for providing stable water channels within the TECs. Hence, TECs with higher PVA concentrations (i.e., the DN-V2, TNV2C1, and TN-V2C2) maintain excellent redox reaction activity due to their ample quantities of –OH groups from the sufficient water channels provided by the PVA.

Further information is provided by the electrochemical impedance spectroscopy (EIS) results in Fig. 4b, and the corresponding equivalent circuit in Fig. S6a. Here, the charge transfer resistance (R_{CT}) and the Warburg element are used to simulate the diffusion resistance (W), while the series resistance of the external circuit (R_S) and the capacitor (C) represent the connected wire and the redox ion electron double-layer behavior near the electrode, respectively. The ionic conductivities were calculated from the intercepts of the tailing lines with the Z' axis, which represent the diffusion impedances of the TECs, and the results are presented in Fig. 4c. Here, the TN-V2C1 TEC exhibits the highest ionic conductivity of 163 mS cm^{-1}, which can be attributed to the large quantity of water channels provided by the optimal amount of PVA, along with the structural integrity provided by the optimal amount of CNF. In view of this result, the TN-V2C1 TEC was selected for the following investigation on the effects of various soaking times on the ionic conductivity and mechanical properties.

The thermogalvanic effect in the TEC is driven by the temperature-dependent electrochemical reaction of the redox couple (Fe(CN)$_6^{3-}$ + e$^-$ ⇌ Fe(CN)$_6^{4-}$) at the two Pt electrodes. The resulting gain and loss of electrons leads to a potential difference across the electrolyte between the hot and cold electrodes, while the consumption of the ions in the redox couple create an ion concentration difference, which promotes the migration of ions between the electrodes. The uninterrupted flow of electrons and the migration of ions enable the thermocell to provide a
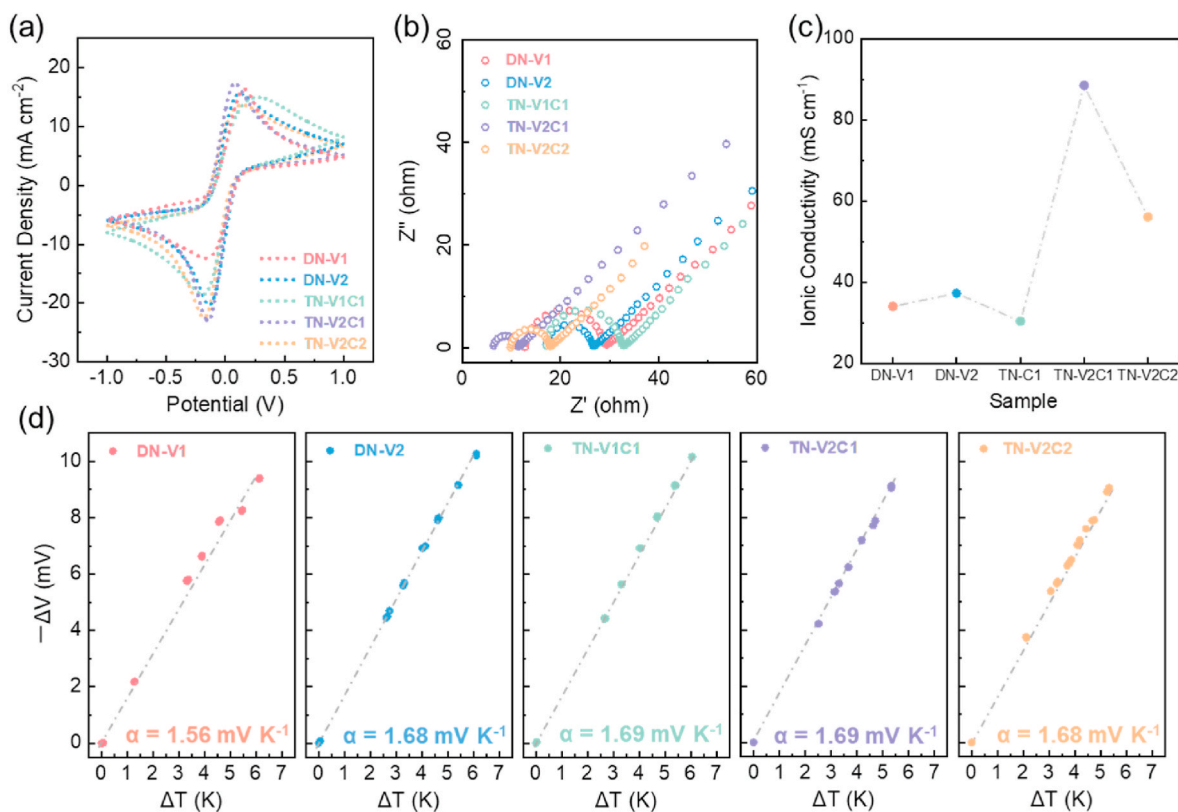

Fig. 4. Electrochemical and TECs properties of TECs. (a) Cyclic voltammetry with the scan rate of 10 mV s^{-1}, (b) Nyquist impedance plot under the frequency from 5 mHz to 1 MHz, (c) σ$_i$ calculated from Nyquist impedance plot and (d) α measurement under the temperature difference from 0 K to 7 K with cold side temperature of 298.15 K.

continuous power supply. The thermopower (α) of the thermogalvanic effect can be expressed as in Equation (1):

$$\alpha = -\frac{\Delta V}{\Delta T} = -\frac{V_H - V_C}{T_H - T_C} \tag{1}$$

where ΔV and ΔT are the respective voltage and temperature differences between the two electrodes, V_H and V_C are the electrical potentials of the hot and cold electrodes respectively, and T_H and T_C are the respective hot and cold terminal temperatures. Thus, the thermoelectrochemical performance of the TEC at redox ion concentrations of 0.42 M and 0.25 M for the $Fe(CN)_6^{4-}$ and $Fe(CN)_6^{3-}$, respectively, are presented in Fig. 4d. Here, the thermopower is seen to remain relatively constant at ~1.68–1.69 mV K^{-1} for most of the TECs, except for the DN-V1 sample. This deviation can be attributed to the less symmetric redox reaction evidenced in this particular electrolyte by the CV results in Fig. 4a. These results suggest that the thermopower of the cell is highly dependent on the specific redox reaction of $Fe(CN)_6^{3-/4-}$ [57,58]. It is noteworthy that the enhancement of redox thermopower can be achieved through solvation shell engineering, which directly influences the entropy change during the redox process. However, it is essential to consider that thermopower is also influenced by the concentration of the redox species. Here, the consistent presence of abundant water in the hydrogels results in similar solvation shells across different samples. Therefore, the absence of variation in concentration among the tested TEC samples contributes to the similar thermopower values.

3.4. Soaking time dependent ionic conductivity and mechanical properties in TN-V2C1 TECs

The effects of various soaking times on the ionic conductivity and mechanical properties of the TN-V2C1 TEC with fixed redox ion concentrations of 0.42 M and 0.25 M for $Fe(CN)_6^{4-}$ and $Fe(CN)_6^{3-}$, respectively, are revealed by the CV measurements in Fig. S6b, . Here, all the TEC samples exhibit similar redox peaks, although the oxidation or reduction peaks of the samples with soaking times of less than 1 h exhibit unexpected shapes. This indicates that the TEC does not become fully saturated with redox ions during the initial hour of soaking.

Meanwhile, the measured thermopowers of the samples with various soaking times are presented in Figs. S7a and b. Here, the thermopower is seen to increase gradually as the soaking time is increased up to 1 h, after which the concentration of redox ions becomes saturated, thus leading to a constant α = thermopower of approximately 1.69 mV K^{-1}. This suggests that the thermopower is highly dependent on the redox reaction of $Fe(CN)_6^{3-/4-}$, and that the saturation of the redox ion concentration plays a crucial role in achieving stable and predictable thermopower values.

The above results are confirmed by the EIS analysis in Fig. 5a, where the TECs that were soaked for less than 1 h (and especially that soaked for 30 s) exhibit a higher impedance, as indicated by the semicircle at high frequency. Moreover, a closer examination of the Nyquist plot in Fig. 5b reveals the presence of both charge transfer (hemisphere) and diffusion (tailing line) impedance for the TECs with less than 1 h of soaking. By contrast, the sample that was soaked for 1 h exhibits the
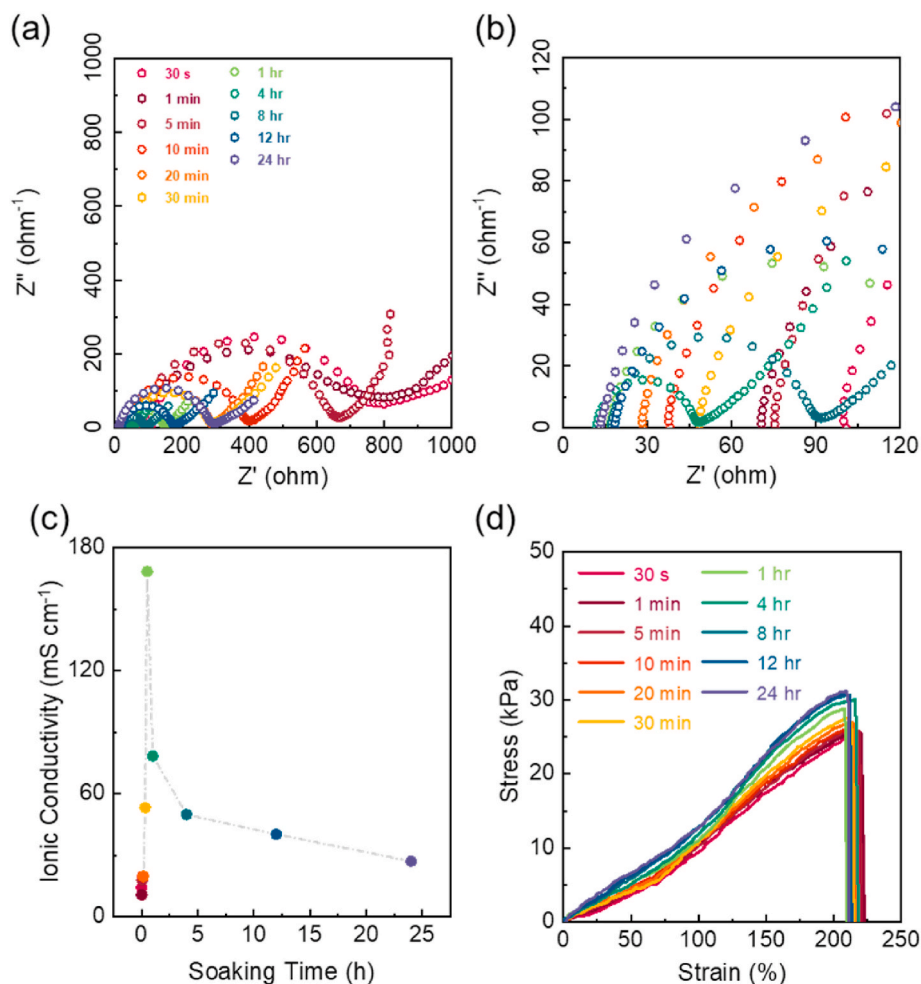

Fig. 5. Electrochemical and mechanical properties of TN-V2C1 TECs in different soaking time. (a) Nyquist impedance plot under the frequency from 5 mHz to 1 MHz, (b) zoom-in Nyquist impedance plot, (c) σ_i calculated from Nyquist impedance plot, and (d) stress-strain curve.

lower charge transfer and diffusion impedance, respectively, along with an enhanced ionic conductivity of 168 mS cm^{-1} (Fig. 5c). The increased ionic conductivity with soaking times of more than 1 h can be attributed to the saturation of ion concentration within the TEC, thereby maximizing the ion transport behavior. Thus, the appropriate soaking time plays a crucial role in facilitating the ion transport behavior and maintaining sufficient redox reactions at the two electrodes. Nevertheless, the results in Fig. 5a–c indicate that the ionic conductivity is decreased when longer soaking times (e.g., above 1 h) are employed, with a larger hemisphere indicating a larger charge transfer impedance, and a larger intercept at the Z' axis indicating significant diffusion impedance. This suggests that prolonged soaking time can lead to the exclusion of water molecules from the TEC, thus resulting in the collapse of water clusters and subsequent suppression of ion transport through the material.

The effects of soaking time on the mechanical properties of the TECs are revealed in Fig. 5d. When the TECs is immersed for less than 1 h, the yield stress is increased from 24.9 to 30.1 kPa, while the tensile strain is decreased from 213 to 210 %. This can be attributed to the exclusion of water molecules from the TEC during soaking. Initially, the polymer chains within the TEC interact with water molecules, which contribute to the flexibility and tensile strain. However, the presence of the redox solution during soaking leads to the exclusion of these water molecules, thereby decreasing the water content of the TEC and allowing the polymer chains to become entangled and develop stronger intermolecular interactions. This, in turn, leads to an increase in the yield stress and a decrease in the tensile strain. Nevertheless, the yield stress and tensile strain values of the TECs remain sufficiently strong for their application and durability in wearable electronics.

3.5. Small-angle X-ray scattering (SAXS) for nanostructure analysis

The nanostructures of the hydrogel samples were characterized by small-angle X-ray scattering (SAXS), as shown in Fig. S8. Here, a synchrotron X-ray source was used to allow for a short collection time, which is particularly beneficial when studying polymer systems with low electron density contrast. For example, the scattering curve of the TN-V2C1 hydrogel sample is shown in Fig. S9a, where two distinct regions (labeled Region I and Region II) are observed and are separated by a knee point at a q_c of approximately 0.01 Å^{-1}. The fractal structures within the double- and triple-network hydrogels can be characterized on a multiscale level using the Beaucage unified equation with R_g represents the radius of gyration and D_f represents the fractal dimension. (see Supplementary information) [59,60].

In Region I ($q < q_c$), the scattering is predominantly influenced by the contribution from global polymer clusters, and the scattering intensity below 0.0025 Å^{-1} displays a Guinier profile (red dots), thus indicating a large-scale inhomogeneous structure characterized by the global radius of gyration ($R_{g, global}$). In the scattering range of 0.0025–0.01 Å^{-1}, however, a power-law intensity profile with I(q) $\sim q^{-D_{f,global}}$ is observed (green dots), indicating a global fractal structure described by the global fractal dimension ($D_{f, global}$). By contrast, the scattering within Region II ($q > q_c$) provides information on the structure of the building blocks that construct the global fractal structure. Here, a Guinier profile (red dots) indicative of a small-scale inhomogeneous structure characterized by the local radius of gyration ($R_{g, local}$) is observed at a scattering intensity of 0.01–0.06 Å^{-1}., while a power-law intensity profile with I(q) $\sim q^{-D_{f,local}}$ (green dots) is observed above 0.06 Å^{-1}, thus suggesting that the building block is also a fractal object characterized by the local fractal dimension ($D_{f, local}$). Notably, the $D_{f, local}$ in Region II approaches 2.0, thus suggesting that the building block resembles a Gaussian coil [61]. Thus, as shown schematically in Fig. S9b, the building block can be visualized as a blob (represented by the blue sphere) containing a polymer chain, and the global network structure is generated by the interconnection of the blobs via the crosslinking reaction. Finally, the proposed structure of the TEC is shown in Fig. S9c, where the redox ions

are assumed to be evenly distributed within the hydrogel matrix.

The SAXS profiles of the various hydrogel samples are shown in Fig. S10a, and the corresponding fittings are presented in Fig. S11a. Thus, the observed scattering curves each display a shoulder at around q = 0.025 Å^{-1} and are well fitted by the two-level unified equation (i.e., Equation (S1)). The resulting $R_{g, local}$, $D_{f, global}$, and $R_{g, global}$ values of the various hydrogel samples are plotted in Figs. S10b–d, respectively. Thus, the $R_{g, global}$ is seen to decrease slightly as the concentration of PVA is increased, from 35.6 Å for the DN-V1 to 32.5 Å for the DN-V2 (Fig. S10b). This can be attributed to the higher crosslinking density attained at a higher polymer concentration, which results in a smaller blob size. Meanwhile, the $D_{f, global}$ values in Fig. S10c can be correlated with the mechanical properties observed in the rheology and stretching analyses (Fig. 3a, S5a, and S5b), as higher $D_{f, global}$ values correspond to a denser network structure and, hence, stronger mechanical properties. Moreover, the addition of CNF is seen to enhance the $D_{f, global}$ value, with the TN-V2C1 hydrogel exhibiting the highest $D_{f, global}$ value of 3.81. Notably, this is close to the value of 4.0 associated with the close packing of the blobs. These results align with the rheology analysis, which showed the largest difference in G′ and G'' values and higher yield stress and tensile strain in the stretching test for TN-V2C1 (Fig. 3a). At the same time, the addition of CNF leads to a decrease in the $R_{g, global}$ from 1532 Å for the DN-V2 to 1499 Å for the TN-V2C1 (Fig. 6d), thus suggesting that the nanofibers fill up any empty spaces in the hydrogel structure.

The TECs scattering curves are presented in Fig. 6a, and the corresponding fitting lines are presented in Fig. S11b. Here, the aggregation shoulders are seen to be reduced in intensity relative to those of the corresponding hydrogels due to the shrinkage of the fractal structure during soaking. Consequently, the $R_{g, local}$ values are found to decrease from 42.4 Å for the TN-V2C1 hydrogel (Fig. S10b) to 29.3 Å for the corresponding TECs (Fig. 6b), and similar trends are observed for the other hydrogels and their corresponding TECs. The water molecules have been partially excluded after soaking into redox ions solution by the osmotic difference and causing the shrinkage of blobs because of the weaker interaction between polymer chains and water molecules. The decrease in the amount of water with increased soaking time is further demonstrated by the wide-angle X-ray scattering (WAXS) analysis in Fig. S12a, where a corresponding decrease the scattering intensity and collapsed water cluster with a shift in the peak position is observed [62, 63]. Nevertheless, the $D_{f, global}$ values of the TECs (Fig. 6c) remain comparable to those of the corresponding hydrogels (Fig. S10c), thus indicating similar mechanical properties. This agrees with the results in Fig. 3a–c, S5a, and S5b), where the TECs exhibit similar yield stresses and only minor decreases in tensile strain compared to the corresponding hydrogel samples. The shrinkage of the blobs and the formation of a condensed structure during soaking of the hydrogels are further revealed by the global size analyses, where the $R_{g, global}$ is seen to decrease from 1499 Å for the TN-V2C1 hydrogel (Fig. S10d) to 1326 Å for the corresponding TECs (Fig. 6d).

The soaking time-dependent nanostructures of the TN-V2C1 TECs are revealed in Fig. 6e, the corresponding scattering curve and fitting line are given in Fig. S11c, and the resulting $R_{g, local}$, $D_{f, global}$, and $R_{g, global}$ values are presented in Fig. 6f–h, respectively. Thus, the $R_{g, local}$ is seen to decrease initially from 36.9 Å to 28.6 Å at the soaking time is increased from 0.5 h to 1 h, thereby indicating a reduction in the blob size (Fig. 6f). With the further increase in soaking time, however, the $R_{g, local}$ remains at around 28 Å, thus suggesting that the TECs have reached a saturation state. A similar trend is observed in the $R_{g, global}$ (Fig. 6h and S12b) with a decrease from 1471 Å at 0.5 h to 1371 Å at 1 h of soaking due to the collapse of the water clusters by osmotic difference. These results indicate the presence of moderate concentrations of redox ions/water molecules within the TECs, which is beneficial for ion transport and is consistent with the abovementioned EIS analysis, where the lower impedance and the highest ionic conductivity of 168 mS cm^{-1} is observed at 1 h (Fig. 5a–c). However, soaking times of more than 1 h
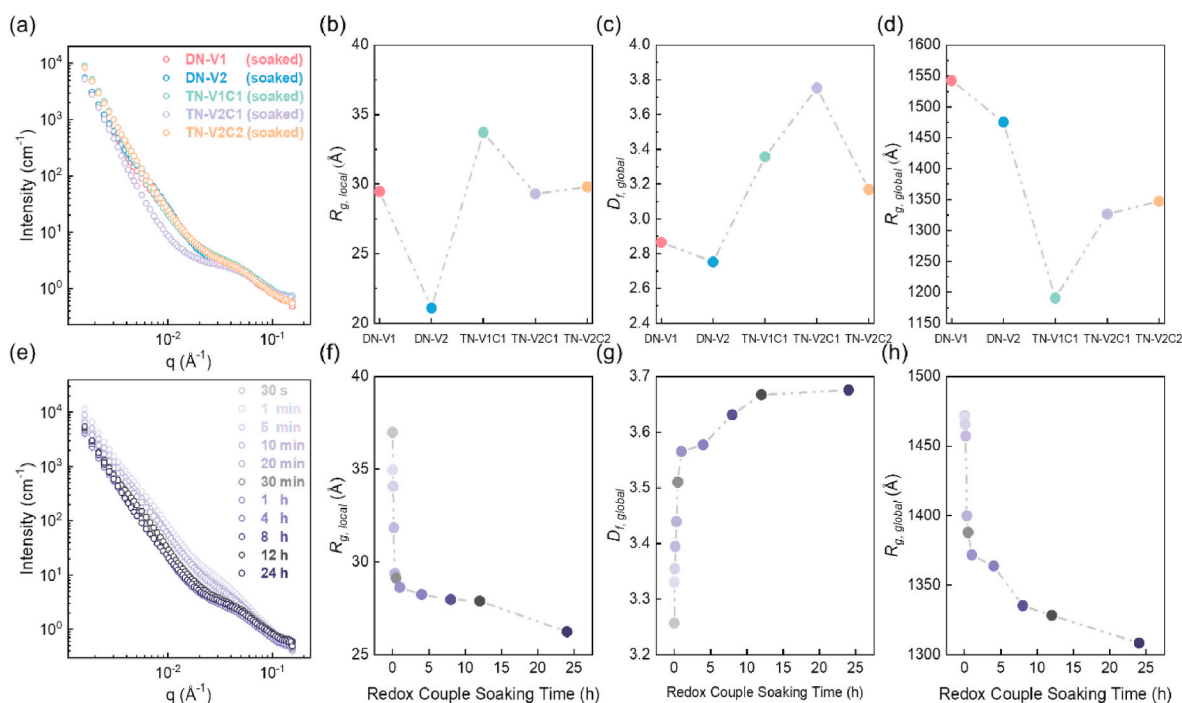
Fig. 6. SAXS analysis of TECs. (a) scattering curves of TECs, (b–d) R_g and D_f values of TECs after soaking 24 h, (e) scattering curves of different soaking time for TN-V2C1 TECs, and (f–h) R_g and D_f values of TN-V2C1 hydrogel-based TECs for different soaking time.

may lead to excessive exclusion of water molecules, thereby suppressing the ionic conductivity. Therefore, a soaking time of 1 h is considered to be optimal, as it provides moderate concentrations of redox ion/water molecules without significantly compromising the ionic conductivity. Moreover, the $D_{f,\ global}$ values are seen to increase slightly from 3.71 at 0.5 h of soaking time to 3.81 at 1 h (Fig. 6g), thereby indicating that the close packing of the blobs results in stronger mechanical properties in agreement with Fig. 3b and c.

The temperature-dependent SAXS analysis of the TN-V2C1 TECs is presented in Figs. S13a–d. Here, the scattering curves show minimal differences in slope and aggregation shoulders across the low q to high q regions, thereby indicating a stable nanostructure. However, some changes in the fitted parameters are observed with the increase in temperature. Specifically, the $R_{g,\ local}$ decreases slightly, from 28.3 to 23.6 Å, as the temperature is increased from 298.15 to 318.15 K (Fig. S13b). This suggests that the polymer chains become more entangled at higher temperatures. Meanwhile, the $D_{f,\ global}$ decreases slightly from 2.96 to 2.85 in the same temperature range (Fig. S13c), while the $R_{g,\ global}$ increases to 1305 Å (Fig. S13d). The latter observation can be attributed to the shorter $R_{g,\ local}$ at higher temperature, which allows more building blocks to participate in the formation of the global fractal structure. However, it is important to note that the changes observed in the temperature dependent SAXS analysis are relatively small compared to the significant effects of the osmotic difference discussed above. These findings suggest that the nanostructure of the TECs remains relatively stable under the working temperature range for TEC applications.

3.6. Perspective on enhanced ionic conductivity and performance comparison of TECs

To overcome the constraints imposed on the transport of redox ions within the polymer matrix, it was imperative to manipulate the nanostructure and water cluster contents of the TECs. As discussed above, the optimization of the nanostructure was achieved by adjustments in both the polymer composition and the duration of redox couple soaking, thereby resulting in a remarkable enhancement in ionic conductivity.

Specifically, the TN-V2C1 TECs exhibit an impressive ionic conductivity of 168 mS cm^{-1} when subjected to a soaking time of 1 h. As revealed by the SAXS and WAXS analyses, the soaking time exerts a considerable influence on the nanostructure, the water cluster content, and the number of redox ions by inducing a denser fractal structure and collapsing the water clusters. The decrease in the quantity of water molecules would lead to shrinkage of the polymer chains and, hence, an increase in surface area, which can facilitate ion transport due to the ample quantity of - OH groups [64,65]. Meanwhile, the amount of water molecules lost can be controlled by using the optimum conditions to provide sufficient redox ion mobility. The above results demonstrate that a soaking time of 1 h for the TN-V2C1 TEC provides the optimum redox ion concentration and amount of water molecules, thereby providing the highest ionic conductivity of 168 mS cm^{-1}.

A comprehensive comparison of the ionic conductivities achieved by the as-prepared and previously-reported TECs systems, encompassing both quasi-solid and aqueous systems, is provided in Fig. 7a and Table S1 [43,44,66–69]. Notably, the TN-V2C1 TECs demonstrate a remarkable ionic conductivity of 168 mS cm^{-1}, surpassing that of the single-network systems, double-network systems, mechanically-trained hydrogel matrices, and even aqueous systems. This can be attributed to the precise control of the nanostructures within the hydrogel matrix. By optimizing the polymer composition and adjusting the redox couple soaking time, the TEC achieves a highly favorable nanostructure that facilitates efficient ion transportation. This advancement in nanostructure engineering contributes significantly to the observed increase in ionic conductivity.

The performance and mechanical properties of the as-optimized TN-V2C1 TEC are compared with those of previously reported devices in Fig. 7b and Table S2 [43,44,67–69]. The corresponding TECs parameters were calculated using Equations (2) and (3)

$$Power\ Factor\ (PF) = \alpha^2 \sigma_i \tag{2}$$

$$Figure\ of\ merit\ (zT) = \frac{PF}{k}T \tag{3}$$

where k is the thermal conductivity and T is the working temperature.
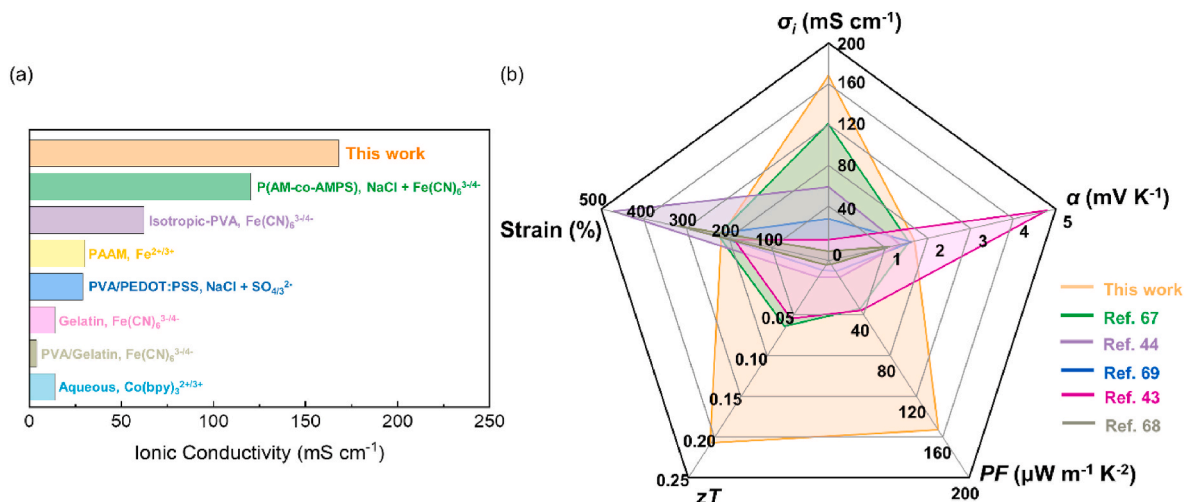
Fig. 7. Comparison in TECs system. (a) σ_i y comparison among quasi-solid TECs system, (b) σ_i, TECs performance and mechanical properties comparison among TGC.

Overall, the as-optimized TN-V2C1 TEC exhibits remarkable performance characteristics, with an impressive ionic conductivity of 168 mS cm^{-1}, along with a competitively moderate thermopower of 1.69 mV K^{-1}, a high *PF* value of 47.9 μW m^{-1} K^{-2}, a high *zT* value of 0.06, and an exceptionally low thermal conductivity of 0.225 W m^{-1} K^{-1}. In terms of mechanical properties, the optimized TN-V2C1 TEC exhibits a moderate tensile strain of 214 %. This exceptional thermoelectrochemical performance clearly highlights the superiority of the as-fabricated TEC.

3.7. Thermoelectric generator (TEG) array and wearable devices applications

The TEG array consisting of nine TN-V2C1 TECs units is shown schematically in Fig. 8a, and optical images are provided in Fig. 8b. Each TEC was sliced and placed in a PDMS mold with dimensions of 1.5×1.5 cm^2 and a thickness of 0.3 cm. Flexible Ni electrodes were used to interconnect the TECs. The TEG array was then encapsulated with thermoconductive tape on the top and bottom surfaces. A custom-built
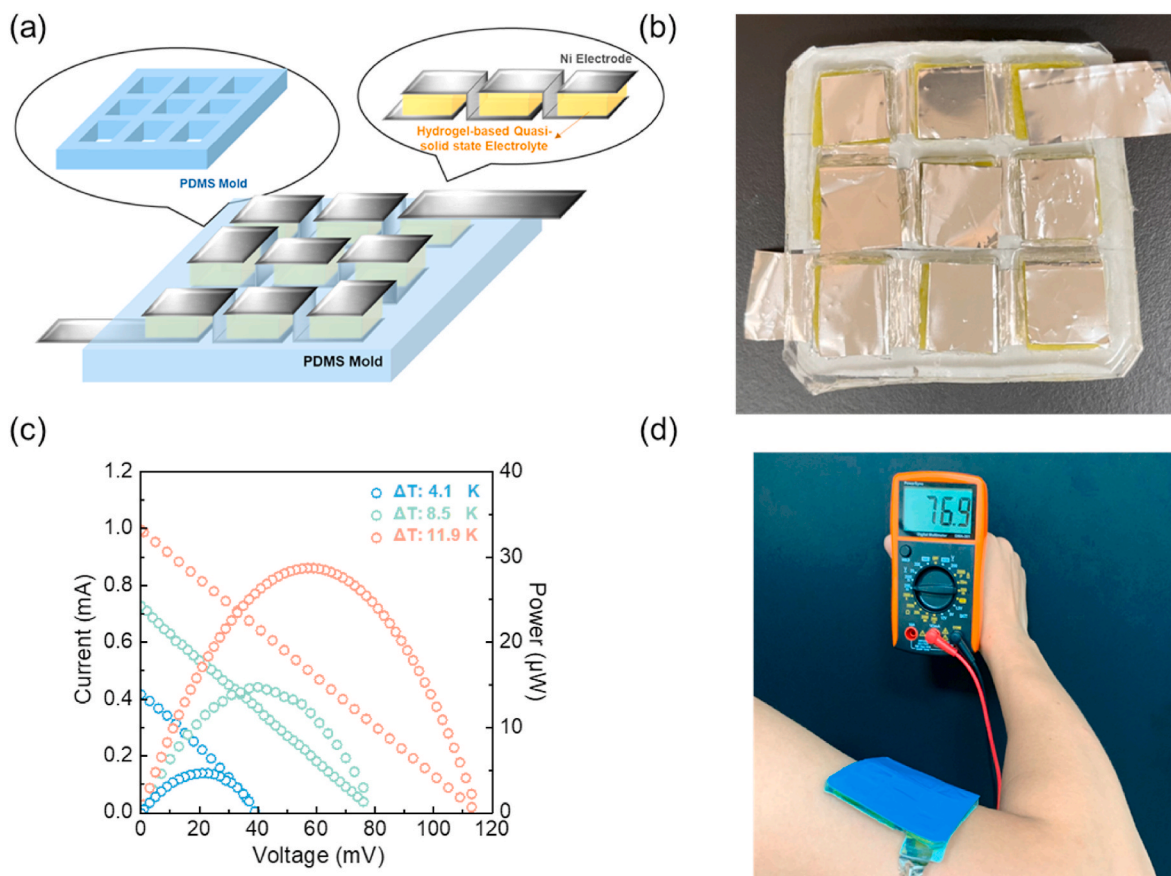

Fig. 8. TEG array performance and wearable device application. (a) schematic illustration of TEG array, (b) optical image of TEG array before encapsulation, (c) TEG array performance, (d) optical image of TEG array for wearable electronics application.

measurement system was employed to evaluate the TEG array, and the performance results are given in Fig. 8c, indicated a high output current of 1.0 mA, an output voltage of 113.1 mV, and a power output of 28.7 μW under a temperature difference of 11.9 K. The power density (P_{max}) is approximately ~ 14.2 mW m^{-2}, resulting in a $P_{max}/\Delta T^2 = 0.1$ mW m^{-2} K^{-2}. The current-voltage curves remain consistent with varying temperature differences, thereby indicating the stability of the TEC performance. However, a slight reduction in the output voltage is observed relative to the thermopower of the TN-V2C1 TEC, which may be attributed to the connecting resistance within the TEG array. Finally, the practical application of the TEG array in wearable devices is demonstrated in Fig. 8d, exhibiting an output voltage of 76.9 mV under ambient temperature conditions of 25 °C and a human skin surface temperature of 35 °C. The thermal image in Fig. 8d captures the real-time temperature during the application of the wearable device. Additionally, Figs. S14a and S14b display output voltage and thermal images of the TEG array positioned above a hotplate with temperature of 308.15 K.

In summary, a TEC with high conductivity was achieved in the present study via control of the hydrogel matrix nanostructure. Moreover, the study demonstrated a high power factor and Figure of merit, along with moderate thermopower and low thermal conductivity. Finally, the TEG array constructed using the TN-V2C1 TEC exhibited tremendous potential for applications in wearable devices.

4. Conclusion

Herein, flexible and stretchable quasi-solid thermo- TECs were successfully fabricated for use as a wearable power supply. The TECs were fabricated using a triple-network hydrogel matrix composed of PAAM/PVA/CNF, which offers excellent mechanical properties and intrinsic stretchability. The Fe(CN)$_6^{3-/4-}$ redox couple was used as a well-known p-type electrolyte due to its suitable thermoelectrochemical performance. By optimization of the TEC, significant results were achieved, including a superior ionic conductivity of 168 mS cm^{-1}, a high power factor of 47.9 μW m^{-1} K^{-2}, and a figure of merit (*zT*) value of 0.06. The exceptional performance was revealed by the utilization of SAXS and WAXS analyses, which provided evidence of a nanostructure that enhances the ion transport capability. To demonstrate the practical application of the TEC, a flexible and stretchable wearable TEG array was fabricated consisting of 9 units of the optimized TECs connected with flexible Ni electrodes, enclosed within a PDMS mold, and secured with thermo-conductive tape. Importantly, the TEG array was designed to conform to the curved surface of the human body. Under a temperature difference of 11.9 K, the TEG array exhibited a high current density of 39.3 μA cm^{-1}, corresponding to an output voltage of 113.1 mV, and a power output of 28.7 μW. When attached to the human skin, the TEG array provided an output voltage of 76.9 mV. This work highlights the potential application of quasi-solid TECs in daily wearable power supply systems, offering low cost, impressive output performance, compact structure, and stretchability. Furthermore, the present findings demonstrate that the unique mechanical properties of the hydrogel matrix open up new possibilities for wearable energy harvesting devices in combination with TECs.

CRediT authorship contribution statement

Yen-Ting Lin: Writing – review & editing, Writing – original draft, Visualization, Validation, Methodology, Investigation, Formal analysis, Data curation, Conceptualization. **Ching-Chieh Hsu:** Writing – review & editing, Methodology, Investigation, Formal analysis, Data curation, Conceptualization. **Shao-Huan Hong:** Methodology, Investigation, Formal analysis, Conceptualization. **Ling-Chieh Lee:** Methodology, Investigation. **U-Ser Jeng:** Resources. **Hsin-Lung Chen:** Methodology, Formal analysis, Data curation. **Shih-Huang Tung:** Investigation, Formal analysis. **Cheng-Liang Liu:** Writing – review & editing,

Supervision, Funding acquisition, Conceptualization.

Declaration of competing interest

The authors declare no conflict of interest.

Data availability

Data will be made available on request.

Appendix A. Supplementary data

Supplementary data to this article can be found online at https://doi.org/10.1016/j.jpowsour.2024.234647.

References

[1] G.R. Chen, Y.Z. Li, M. Bick, J. Chen, Smart textiles for electricity generation, Chem. Rev. 120 (2020) 3668–3720. https://10.1021/acs.chemrev.9b00821.

[2] Y. Guan, J. Yan, Y. Shan, Y. Zhou, Y. Hang, R. Li, Burden of the global energy price crisis on households, Nat. Energy 8 (2023) 304–316. https://10.1038/s41560-023-01209-8.

[3] H. Cheng, J. Ouyang, Soret effect of ionic liquid gels for thermoelectric conversion, J. Phys. Chem. Lett. 13 (2022) 10830–10842. https://10.1021/acs.jpclett.2c02645.

[4] Y. Liu, H. Wang, P.C. Sherrell, L. Liu, Y. Wang, J. Chen, Potentially wearable thermoelectrochemical cells for body heat harvesting: from mechanism, materials, strategies to applications, Adv. Sci. 8 (2021) 2100669. https://10.1002/advs.202100669.

[5] M. Massetti, F. Jiao, A.J. Ferguson, D. Zhao, K. Wijeratne, A. Würger, Unconventional thermoelectric materials for energy harvesting and sensing applications, Chem. Rev. 121 (2021) 12465–12547. https://10.1021/acs.chemrev.1c00218.

[6] Y. Pang, Y. Cao, M. Derakhshani, Y. Fang, Z.L. Wang, C. Cao, Hybrid energy-harvesting systems based on triboelectric nanogenerators, Matter 4 (2021) 116–143. https://10.1016/j.matt.2020.10.018.

[7] J. He, T.M. Tritt, Advances in thermoelectric materials research: looking back and moving forward, Science 357 (2017) eaak9997. https://10.1126/science.aak9997.

[8] X.L. Shi, J. Zou, Z.G. Chen, Advanced thermoelectric design: from materials and structures to devices, Chem. Rev. 120 (2020) 7399–7515. https://10.1021/acs.chemrev.0c00026.

[9] L. Yang, Z.G. Chen, M.S. Dargusch, J. Zou, High performance thermoelectric materials: progress and their applications, Adv. Energy Mater. 8 (2018) 1701797. https://10.1002/aenm.201701797.

[10] Y.-H. Pai, J. Tang, Y. Zhao, Z. Liang, Ionic organic thermoelectrics with impressively high thermopower for sensitive heat harvesting scenarios, Adv. Energy Mater. 13 (2023) 2202507. https://10.1002/aenm.202202507.

[11] D. Zhao, A. Würger, X. Crispin, Ionic thermoelectric materials and devices, J. Energy Chem. 61 (2021) 88–103. https://10.1016/j.jechem.2021.02.022.

[12] M. Hirschberger, S. Kushwaha, Z.J. Wang, Q. Gibson, S.H. Liang, C.A. Belvin, The chiral anomaly and thermopower of weyl fermions in the half-heusler gdptbi, Nat. Mater. 15 (2016) 1161–1165. https://10.1038/NMAT4684.

[13] W.G. Zeier, J. Schmitt, G. Hautier, U. Aydemir, Z.M. Gibbs, C. Felser, Engineering half-heusler thermoelectric materials using zintl chemistry, Nat. Rev. Mater. 1 (2016) 16032. https://10.1038/natrevmats.2016.32.

[14] S.L. Zhang, S.Y. Guo, Z.F. Chen, Y.L. Wang, H.J. Gao, J. Gomez-Herrero, Recent progress in 2d group-va semiconductors: from theory to experiment, Chem. Soc. Rev. 47 (2018) 982–1021. https://10.1039/c7cs00125h.

[15] G. Chen, R. Rastak, Y. Wang, H. Yan, V. Feig, Y. Liu, Strain- and strain-rate-invariant conductance in a stretchable and compressible 3d conducting polymer foam, Matter 1 (2019) 205–218. https://10.1016/j.matt.2019.03.011.

[16] M. Zhu, X.-L. Shi, H. Wu, Q. Liu, Z.-G. Chen, Advances in ag2s-based thermoelectrics for wearable electronics: progress and perspective, Chem. Eng. J. 473 (2023) 145236. https://10.1016/j.cej.2023.145236.

[17] C. Chang, M.H. Wu, D.S. He, Y.L. Pei, C.F. Wu, X.F. Wu, 3d charge and 2d phonon transports leading to high out-of-plane zt in n-type snse crystals, Science 360 (2018) 778–782. https://10.1126/science.aaq1479.

[18] B.B. Jiang, Y. Yu, J. Cui, X.X. Liu, L. Xie, J.C. Liao, High-entropy-stabilized chalcogenides with high thermoelectric performance, Science 371 (2021) 830–834. https://10.1126/science.abe1292.

[19] J. Mao, H.T. Zhu, Z.W. Ding, Z.H. Liu, G.A. Gamage, G. Chen, High thermoelectric cooling performance of n-type mg3bi2-based materials, Science 365 (2019) 495–498. https://10.1126/science.aax7792.

[20] I.T. Witting, T.C. Chasapis, F. Ricci, M. Peters, N.A. Heinz, G. Hautier, The thermoelectric properties of bismuth telluride, Adv. Electron. Mater. 5 (2019) 1800904. https://10.1002/aelm.201800904.

[21] C.J. Zhou, Y.K. Lee, Y. Yu, S. Byun, Z.Z. Luo, H. Lee, Polycrystalline snse with a thermoelectric figure of merit greater than the single crystal, Nat. Mater. 20 (2021) 1378–1384. https://10.1038/s41563-021-01064-6.

[22] J.L. Blackburn, A.J. Ferguson, C. Cho, J.C. Grunlan, Carbon-nanotube-based thermoelectric materials and devices, Adv. Mater. 30 (2018) 1704386. https://10.1002/adma.201704386.

[23] X. Fan, W.Y. Nie, S.H. Tsai, N.X. Wang, H.H. Huang, Y.J. Cheng, Pedot:Pss for flexible and stretchable thermoelectrics: modifications, strategies, and applications, Adv. Sci. 6 (2019) 1900813. https://10.1002/advs.201900813.

[24] Y.H. Jia, Q.L. Jiang, H.D. Sun, P.P. Liu, D.H. Hu, Y.Z. Pei, Wearable thermoelectric materials and devices for self-powered electronic systems, Adv. Mater. 33 (2021) 2102990. https://10.1002/adma.202102990.

[25] L. Zhang, X.L. Shi, Y.L. Yang, Z.G. Chen, Flexible thermoelectric materials and devices: from materials to applications, Mater. Today 46 (2021) 62–108. https://10.1016/j.mattod.2021.02.016.

[26] Y. Hao, X. He, L. Wang, X. Qin, G. Chen, J. Yu, Stretchable thermoelectrics: strategies, performances, and applications, Adv. Funct. Mater. 32 (2022) 2109790. https://10.1002/adfm.202109790.

[27] N. Nandihalli, C.-J. Liu, T. Mori, Polymer based thermoelectric nanocomposite materials and devices: fabrication and characteristics, Nano Energy 78 (2020) 105186. https://10.1016/j.nanoen.2020.105186.

[28] T.J. Abraham, D.R. MacFarlane, J.M. Pringle, High seebeck coefficient redox ionic liquid electrolytes for thermal energy harvesting, Energy Environ. Sci. 6 (2013) 2639–2645. https://10.1039/c3ee41608a.

[29] M.F. Dupont, D.R. MacFarlane, J.M. Pringle, Thermo-electrochemical cells for waste heat harvesting - progress and perspectives, Chem. Commun. 53 (2017) 6288–6302. https://10.1039/c7cc02160g.

[30] M.A. Lazar, D. Al-Masri, D.R. MacFarlane, J.M. Pringle, Enhanced thermal energy harvesting performance of a cobalt redox couple in ionic liquid-solvent mixtures, Phys. Chem. Chem. Phys. 18 (2016) 1404–1410. https://10.1039/c5cp04305k.

[31] L.R. Liang, H.C. Lv, X.L. Shi, Z.X. Liu, G.M. Chen, Z.G. Chen, A flexible quasi-solid-state thermoelectrochemical cell with high stretchability as an energy-autonomous strain sensor, Mater. Horiz. 8 (2021) 2750–2760. https://10.1039/d1mh00775k.

[32] Y.Q. Liu, H.B. Wang, P.C. Sherrell, L.L. Liu, Y. Wang, J. Chen, Potentially wearable thermo-electrochemical cells for body heat harvesting: from mechanism, materials, strategies to applications, Adv. Sci. 8 (2021) 2100669. https://10.1002/advs.202100669.

[33] M. Rahimi, A.P. Straub, F. Zhang, X. Zhu, M. Elimelech, C.A. Gorski, Emerging electrochemical and membrane-based systems to convert low-grade heat to electricity, Energy Environ. Sci. 11 (2018) 276–285. https://10.1039/c7ee03026f.

[34] X. Wang, Y.T. Huang, C. Liu, K.Y. Mu, K.H. Li, S.J. Wang, Direct thermal charging cell for converting low-grade heat to electricity, Nat. Commun. 10 (2019) 4151. https://10.1038/s41467-019-12144-2.

[35] J. Wu, J.J. Black, L. Aldous, Thermoelectrochemistry using conventional and novel gelled electrolytes in heat-to-current thermocells, Electrochim. Acta 225 (2017) 482–492. https://10.1016/j.electacta.2016.12.152.

[36] R. Hu, D. Xu, X. Luo, Liquid thermocells enable low-grade heat harvesting, Matter 3 (2020) 1400–1402. https://10.1016/j.matt.2020.10.008.

[37] W. Gao, H. Meng, Y. Chen, X. Liu, Quasi-solid n-type thermogalvanic thermocells with enhanced ionic conductivity for continuous low-grade heat harvesting, Appl. Phys. Lett. 121 (2022) 203902. https://10.1063/5.0120728.

[38] J.G. Jeon, H.J. Kim, G. Shin, Y. Han, J.H. Kim, J.H. Lee, High-precision ionic thermocouples fabricated using potassium ferri/ferrocyanide and iron perchlorate, Adv. Electron. Mater. 8 (2022) 2100693. https://10.1002/aelm.202100693.

[39] Y. Liu, S. Zhang, Y. Zhou, M.A. Buckingham, L. Aldous, P.C. Sherrell, Advanced wearable thermocells for body heat harvesting, Adv. Energy Mater. 10 (2020) 2002539. https://10.1002/aenm.202002539.

[40] H. Wang, X. Zhuang, W. Xie, H. Jin, R. Liu, B. Yu, Thermosensitive-csi3-crystal-driven high-power i−/i3− thermocells, Cell Rep. Phys. Sci. 3 (2022) 100737. https://10.1016/j.xcrp.2022.100737.

[41] J. Duan, B. Yu, K. Liu, J. Li, P. Yang, W. Xie, P-n conversion in thermogalvanic cells induced by thermo-sensitive nanogels for body heat harvesting, Nano Energy 57 (2019) 473–479. https://10.1016/j.nanoen.2018.12.073.

[42] A. Taheri, D.R. MacFarlane, C. Pozo-Gonzalo, J.M. Pringle, Quasi-solid-state electrolytes for low-grade thermal energy harvesting using a cobalt redox couple, ChemSusChem 11 (2018) 2788–2796. https://doi.org/10.1002/cssc.201800794.

[43] C.-G. Han, X. Qian, Q. Li, B. Deng, Y. Zhu, Z. Han, Giant thermopower of ionic gelatin near room temperature, Science 368 (2020) 1091–1098. https://10.1126/science.aaz5045.

[44] Z. Lei, W. Gao, W. Zhu, P. Wu, Anti-fatigue and highly conductive thermocells for continuous electricity generation, Adv. Funct. Mater. 32 (2022) 2201021. https://10.1002/adfm.202201021.

[45] P. Peng, Z. Li, D. Xie, K. Zhu, C. Du, L. Liang, Aqueous eutectic hydrogel electrolytes enable flexible thermocells with a wide operating temperature range, J. Mater. Chem. A 11 (2023) 6986–6996. https://10.1039/d2ta09385e.

[46] P. Peng, J. Zhou, L. Liang, X. Huang, H. Lv, Z. Liu, Regulating thermogalvanic effect and mechanical robustness via redox ions for flexible quasi-solid-state thermocells, Nano-Micro Lett. 14 (2022) 81. https://10.1007/s40820-022-0082 4-6.

[47] P. Yin, Y. Geng, L. Zhao, Q. Meng, Z. Xin, L. Luo, Robust and flexible bacterial cellulose-based thermogalvanic cells for low-grade heat harvesting in extreme environments, Chem. Eng. J. 457 (2023) 141274. https://10.1016/j.cej.2023.141 274.

[48] Y. Zong, H. Li, X. Li, J. Lou, Q. Ding, Z. Liu, Bacterial cellulose-based hydrogel thermocells for low-grade heat harvesting, Chem. Eng. J. 433 (2022) 134550. http s://10.1016/j.cej.2022.134550.

[49] J. Shen, Y. Ma, C. Yang, S. Liu, J. Li, Z. Chen, Boosting solar-thermal-electric conversion of thermoelectrochemical cells by construction of a carboxymethylcellulose-interpenetrated polyacrylamide network, J. Mater. Chem. A 10 (2022) 7785–7791. https://10.1039/d2ta00025c.

[50] Y. Shi, B. Wu, S. Sun, P. Wu, Aqueous spinning of robust, self-healable, and crack-resistant hydrogel microfibers enabled by hydrogen bond nanoconfinement, Nat. Commun. 14 (2023) 1370. https://10.1038/s41467-023-37036-4.

[51] X. Shi, L. Ma, Y. Li, Z. Shi, Q. Wei, G. Ma, Double hydrogen-bonding reinforced high-performance supramolecular hydrogel thermocell for self-powered sensing remote-controlled by light, Adv. Funct. Mater. 33 (2023) 2211720. https://10.1002/adfm.202211720.

[52] W. Gao, Z. Lei, W. Chen, Y. Chen, Hierarchically anisotropic networks to decouple mechanical and ionic properties for high-performance quasi-solid thermocells, ACS Nano 16 (2022) 8347–8357. https://10.1021/acsnano.2c02606.

[53] J.H. Kim, Y. Han, G. Shin, J.G. Jeon, H.J. Kim, B.J. So, Separation-free planar interconnection for thermo-electrochemical cells, ACS Appl. Energy Mater. 5 (2022) 13053–13061. https://10.1021/acsaem.2c02778.

[54] S. Pu, Y. Liao, K. Chen, J. Fu, S. Zhang, L. Ge, Thermogalvanic hydrogel for synchronous evaporative cooling and low-grade heat energy harvesting, Nano Lett. 20 (2020) 3791–3797. https://10.1021/acs.nanolett.0c00800.

[55] Y. Liu, M. Cui, W. Ling, L. Cheng, H. Lei, W. Li, Thermo-electrochemical cells for heat to electricity conversion: from mechanisms, materials, strategies to applications, Energy Environ. Sci. 15 (2022) 3670–3687. https://10.1039/D 2EE01457B.

[56] H. Cheng, Q. Le, Z. Liu, Q. Qian, Y. Zhao, J. Ouyang, Ionic thermoelectrics: principles, materials and applications, J. Mater. Chem. C 10 (2022) 433–450. https://10.1039/D1TC05242J.

[57] M. Li, M. Hong, M. Dargusch, J. Zou, Z.-G. Chen, High-efficiency thermocells driven by thermo-electrochemical processes, Trends Chem 3 (2021) 561–574. https://10.1016/j.trechm.2020.11.001.

[58] Y. Liu, H. Wang, P.C. Sherrell, L. Liu, Y. Wang, J. Chen, Potentially wearable thermo-electrochemical cells for body heat harvesting: from mechanism, materials, strategies to applications, Adv. Sci. 8 (2021) 2100669. https://10.1002/advs.202100669.

[59] A. Forgacs, V. Papp, G. Paul, L. Marchese, A. Len, Z. Dudas, Mechanism of hydration and hydration induced structural changes of calcium alginate aerogel, ACS Appl. Mater. Interfaces 13 (2021) 2997–3010. https://10.1021/acsami.0c17012.

[60] B. Wu, M. Siglreitmeier, C. Debus, D. Schwahn, H. Colfen, V. Pipich, Ionic dependence of gelatin hydrogel architecture explored using small and very small angle neutron scattering technique, Macromol. Biosci. 18 (2018) e1800018. https://10.1002/mabi.201800018.

[61] O. Kuzminskaya, S. Riemer, R. Dalgliesh, L. Almásy, I. Hoffmann, M. Gradzielski, Structure and phase behavior of interpolyelectrolyte complexes of pdadmac and hydrophobically modified paa (hm-paa), Macromol. Chem. Phys. 224 (2022) 2200276. https://10.1002/macp.202200276.

[62] V.V. Atrazhev, T.Y. Astakhova, V.I. Sultanov, M.L. Perry, S.F. Burlatsky, Molecular dynamic study of water-cluster structure in pfsa and pfia ionomers, J. Electrochem. Soc. 164 (2017) F1265. https://10.1149/2.0041713jes.

[63] J.H. Hack, J.P. Dombrowski, X. Ma, Y. Chen, N.H.C. Lewis, W.B. Carpenter, Structural characterization of protonated water clusters confined in hzsm-5 zeolites, J. Am. Chem. Soc. 143 (2021) 10203–10213. https://10.1021/jacs.1c 03205.

[64] F. Mo, Z. Chen, G. Liang, D. Wang, Y. Zhao, H. Li, Zwitterionic sulfobetaine hydrogel electrolyte building separated positive/negative ion migration channels for aqueous zn-mno2 batteries with superior rate capabilities, Adv. Energy Mater. 10 (2020) 2000035. https://10.1002/aenm.202000035.

[65] M. Yao, B. Wu, X. Feng, S. Sun, P. Wu, A highly robust ionotronic fiber with unprecedented mechanomodulation of ionic conduction, Adv. Mater. 33 (2021) e2103755. https://10.1002/adma.202103755.

[66] Y. Ikeda, Y. Cho, Y. Murakami, Thermogalvanic energy harvesting from forced convection cooling of 100–200 °c surfaces generating high power density, Sustain. Energy Fuels 5 (2021) 5967–5974. https://10.1039/d1se01264a.

[67] Z. Lei, W. Gao, P. Wu, Double-network thermocells with extraordinary toughness and boosted power density for continuous heat harvesting, Joule 5 (2021) 2211–2222. https://10.1016/j.joule.2021.06.003.

[68] X. Li, J. Li, T. Wang, S.A. Khan, Z. Yuan, Y. Yin, Self-powered respiratory monitoring strategy based on adaptive dual-network thermogalvanic hydrogels, ACS Appl. Mater. Interfaces 14 (2022) 48743–48751. https://10.1021/acsami. 2c14239.

[69] C. Tian, C. Bai, T. Wang, Z. Yan, Z. Zhang, K. Zhuo, Thermogalvanic hydrogel electrolyte for harvesting biothermal energy enabled by a novel redox couple of $SO_{4/3}^{2-}$ ions, Nano Energy 106 (2023) 108077. https://10.1016/j.nanoen.2022.10 8077.